Journal of Magnetism and Magnetic Materials 633 (2025) 173553

Contents lists available at ScienceDirect

Journal of Magnetism and Magnetic Materials

journal homepage: www.elsevier.com/locate/jmmm

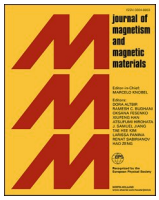

Influence of molybdenum substitution on the magnetic characteristics of calcium-based MOFs

P. Arularasan [a], Saravanan Pandiaraj [b,c], P. Rajesh [d], M. Pavithra [e], G.N. Dar [f], S.R. Majid [g,*], Mohd Arif Dar [g,h,**]

[a] Department of Physics, Dwaraka Doss Goverdhan Doss Vaishnav College, Chennai, Tamil Nadu 600107, India
[b] Department of Self-Development Skills, King Saud University, P.O. Box 2455, 11451 Riyadh, Saudi Arabia
[c] King Salman Center for Disability Research, 11614 Riyadh, Saudi Arabia
[d] Department of Physics, School of Basic Science, Vels Institute of Science and Technology & Advanced Studies, Pallavaram, Chennai, Tamil Nadu 600117, India
[e] Department of Condensed Matter Physics, Saveetha School of Engineering, Saveetha Institute of Medical and Technical Sciences (SIMATS), Chennai, Tamil Nadu 602105, India
[f] Department of Physics, University of Kashmir, Srinagar 190006, Jammu and Kashmir, India
[g] Centre for Ionics, Department of Physics, Universiti Malaya, 50603 Kuala Lumpur, Malaysia
[h] Faculty of Allied Health Sciences, Chettinad Hospital, and Research Institute, Chettinad Academy of Research and Education, Kelambakkam 603103, Tamil Nadu, India

ARTICLE INFO

Keywords:
LaCaMo
XRD
Polycrystalline phase
Soft ferromagnetic behavior

ABSTRACT

In this study, a novel series of LaCaMo-based metal-organic framework (MOF) materials was synthesized and named LCM1, LCM2, LCM3 and LCM4 MOFs. The X-ray diffraction (XRD) confirmed the formation of a single-phase tetragonal scheelite-type structure with a crystalline size of 12, 30, 37 and 67 (nm). The FTIR spectra show the peaks of Mo—O at 733 and 766 (cm^{-1}) and a band observed at 425 and 527 (cm^{-1}) corresponds to the absorption of Ca—O. The scanning electron microscopy (SEM) and transmission electron microscopy (TEM) show the spherical agglomerated images with increasing diameter. The selected area electron dispersive (SAED) analyses confirmed high polycrystalline phase purity. The XPS spectra validated the oxidation states of Ca^{2+}, Mo^{6+}, and La^{3+} elements, confirming the substitution of La ions for CaMo MOF. The magnetic measurements using vibrating sample magnetometry revealed a systematic increase in magnetization (0.002 to 0.018 emu/g) from LCM1 to LCM4 MOFs, indicating soft ferromagnetic behavior.

1. Introduction

MOFs are a class of crystalline materials constructed from metal ions or clusters coordinated with organic ligands to form porous networks [1]. These materials have attracted immense interest due to their remarkable structural tunability, high surface area, and diverse functionalities, finding applications in gas storage, separation, catalysis, drug delivery, sensing, and magnetism [2]. Among various MOFs, calcium-based MOFs (Ca-MOFs) are emerging as promising candidates for magnetic, biomedical, and environmental applications owing to the abundance, biocompatibility, and low toxicity of calcium ions. However, Ca^{2+} typically exists as a diamagnetic ion with a closed-shell configuration, which limits its magnetic properties. The introduction of molybdenum into Ca-MOFs can induce substantial changes in their electronic and magnetic behavior due to the distinct electronic configuration and multiple oxidation states of molybdenum ions [3]. As a 4d transition metal, molybdenum (Mo) can exhibit unpaired electrons, leading to paramagnetic or ferromagnetic behavior, and its incorporation into the MOF framework introduces local magnetic moments that may couple through organic linkers to generate long-range magnetic ordering or complex magnetic phenomena [4]. In addition, Mo substitution can influence the structural and electronic properties of the MOF, indirectly affecting magnetic interactions [5].

Mo substitution has been extensively employed to tailor the electronic, catalytic, and magnetic properties of metal oxides and hybrid frameworks. In ferrites and transition-metal oxides, Mo incorporation enhances magnetic coupling, coercivity, and superparamagnetic behavior, highlighting its role as an effective dopant. Extending this

* Corresponding author.
** Corresponding author at: Centre for Ionics, Department of Physics, Universiti Malaya, 50603 Kuala Lumpur, Malaysia.
E-mail addresses: shana@um.edu.my (S.R. Majid), dararifphy@gmail.com (M.A. Dar).

https://doi.org/10.1016/j.jmmm.2025.173553
Received 1 July 2025; Received in revised form 16 September 2025; Accepted 26 September 2025
Available online 27 September 2025

strategy to calcium-based MOFs offers a new route to engineer magnetic functionality. In MOFs, magnetic behavior originates from unpaired electrons in the metal centers and their exchange interactions mediated by organic linkers, with Fe, Co, Ni, Mn, Cu, and rare earth elements exhibiting phenomena such as ferromagnetism, antiferromagnetism, superparamagnetism, and single-molecule magnetism [6]. The substitution of Mo in Ca-MOFs can introduce localized magnetic moments that interact through organic bridges, potentially giving rise to complex responses such as spin-glass states, metamagnetic transitions, or weak ferromagnetism [7]. These effects are highly sensitive to Mo concentration, oxidation state, distribution uniformity, and coordination geometry. At low substitution levels, isolated paramagnetic centers dominate, whereas higher concentrations promote spin–spin interactions and long-range ordering [8]. In addition, Mo incorporation can modify the electronic structure of Ca-MOFs by introducing states near the Fermi level, thereby influencing band dispersion, charge transport, and indirectly, magnetic interactions in low-dimensional or conjugated systems [9,10]. Thus, Mo-doped Ca-MOFs emerge as multifunctional candidates with coupled magnetic and electronic properties.

To the best of our knowledge, no systematic studies have yet been reported on calcium-based MOFs. Thus, this study aims to synthesize La-substituted CaMo MOFs. The synthesized MOFs are coded LCM1, LCM2, LCM3, and LCM4 MOFs, and their structural, morphological, surface, and magnetic properties are investigated. The LCM1, LCM2, LCM3, and LCM4 MOFs were investigated using XRD, FT-Raman, FTIR, XPS, SEM, and TEM studies. Among all these synthesized MOFs, the LCM4 series exhibits the most promising magnetic behavior, demonstrating strong magnetic ordering, enhanced magnetic susceptibility, and thermal stability. These magnetic enhancements are attributed to the synergistic interplay between La, Ca, and Mo ions, the presence of oxygen vacancies that influence spin alignment.

2. Experimental section

2.1. Materials

Calcium nitrate tetrahydrate [$Ca(NO_3)_2{\cdot}4H_2O$], lanthanum nitrate hexahydrate [$La(NO_3)_3{\cdot}6H_2O$], sodium molybdate dihydrate [$Na_2MoO_4{\cdot}2H_2O$], and 2-methylimidazole ($C_4H_6N_2$), were obtained from Sigma-Aldrich and used as received without further purification. The distilled water and ethanol were purchased from Hyma Chemicals and used as solvents throughout the synthesis.

2.2. Synthesis of La_xCaMo_{1-x} MOF

A series of La_xCaMo_{1-x} MOFs was synthesized via a precipitation route, wherein the calcium source was maintained at a fixed concentration, and the ratios of lanthanum and molybdate precursors were systematically varied to investigate their influence on MOF formation and crystallinity. Initially, 1 M calcium nitrate tetrahydrate was dissolved in 25 mL of distilled water under constant magnetic stirring at ambient temperature. In parallel, aqueous solutions of lanthanum nitrate hexahydrate and sodium molybdate dihydrate were prepared in equimolar volumes (25 mL each) at concentrations described in Table 1. Each lanthanum–molybdate solution (50 mL) was added dropwise to the calcium nitrate solution (25 mL) under magnetic stirring, followed by the addition of 0.1 M 2-methylimidazole to the resulting 75 mL reaction mixture. The solution was stirred continuously for 30 min at room temperature to ensure uniform mixing and precursor complexation. The homogeneous solution was subsequently kept under magnetic stirring at 60 °C for 2 h under stirring conditions. The resulting precipitate was collected, washed repeatedly with ethanol, and finally dried in a hot air oven at 80 °C overnight. The obtained materials were labelled according to the precursor ratio as La_xCaMo_{1-x} MOFs, coded LCM1, LCM2, LCM3, and LCM4 MOFs.

Table 1
Different ratios of lanthanum nitrate and sodium molybdate.

Sample Code	$[La(NO_3)_3]$ (M)	$[Na_2MoO_4]$ (M)
LCM1	0.1 (1 %)	0.9 (99 %)
LCM2	0.2 (2 %)	0.8 (98 %)
LCM3	0.3 (3 %)	0.7 (97 %)
LCM4	0.4 (4 %)	0.6 (96 %)

2.3. Materials characterization

The phase purity of the synthesized materials was confirmed by XRD using a Bruker D8 diffractometer equipped with Cu-Kα radiation (λ = 1.514 Å). The FTIR spectra were recorded using a PerkinElmer spectrometer to identify functional groups. The Raman spectra were obtained using a Bruker RFS 27 spectrometer. The surface morphology and microstructure were examined using SEM (Zeiss Scanning Electron Microscope) and high-resolution transmission electron microscopy (HR-TEM, JEM-2100 Plus). The surface chemical composition and oxidation states of the elements were analyzed using XPS (Thermo Fisher Scientific K-Alpha). The Lakeshore 7410 vibrating sample magnetometer (VSM) was used to analyse the magnetic properties of the sample through VSM studies.

3. Results and Discussion

XRD analysis was performed to determine the phase purity, crystal structure, and crystallinity of the synthesized LCM1, LCM2, LCM3, and LCM4 MOFs. Fig. 1 shows the XRD spectra of the LCM1, LCM2, LCM3 and LCM4 MOFs. The XRD spectra of the LCM1, LCM2, LCM3 and LCM4 MOFs displayed sharp, well-resolved diffraction peaks without any indication of impurity phases, confirming their high crystallinity and single-phase nature. The patterns were matched using X'Pert HighScore software with the JCPDS database and showed excellent agreement with the standard pattern for calcium molybdate ($CaMoO_4$), corresponding to Reference code: 96-157-0755. This phase is known as powellite, which crystallizes in a tetragonal scheelite-type structure with space group $I4_1/a$ (No. 88), a well-established framework for molybdate materials [11–13]. The XRD does not show any La peaks, indicating that La^{3+} ions can be successfully substituted into Ca^{2+} sites without causing significant lattice distortion. This substitution is structurally tolerated due to the close ionic radii of La^{3+} (1.16 Å) and Ca^{2+} (1.12 Å) in eightfold coordination [14,15]. Notably, the XRD patterns of LCM2 also matched ICSD code 060552, which includes patterns obtained under non-

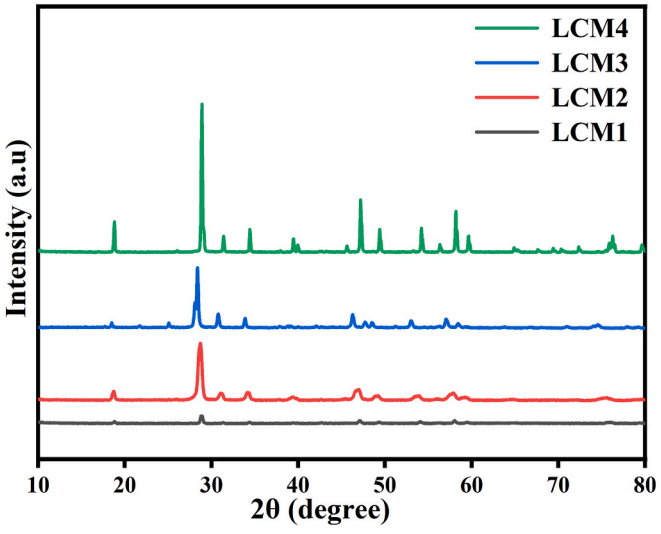

Fig. 1. XRD spectra of the LCM1, LCM2, LCM3 and LCM4 MOFs.

ambient conditions, suggesting high structural stability even under potential synthesis-related strain. The most intense diffraction peak for all samples was consistently observed at 2θ ≈ 28.8°, corresponding to the (112) plane of the tetragonal $CaMoO_4$ structure. Additional reflections appearing at 18.86°, 31.18°, 34.35°, 39.22°, 47.11°, 49.25°, 53.83°, 59.28°, 75.95°, 79.42°, 80.60°, and 82.08 were indexed to (011), (004), (020), (211), (024), (220), (031), (017), (141), (332), (037) and (420) planes, respectively. The absence of peak splitting or shifting beyond 0.05° indicates uniform lattice parameters across the series, implying the successful formation of LaCaMo solid solutions without phase separation [16]. The slight variations in peak intensity among LCM1 to LCM4 could be attributed to differences in preferred orientation, local strain, or crystallite size distributions. Using the following equations.

Debye Scherrer eq

$$D = \frac{n\lambda}{\beta Cos\theta} \tag{1}$$

Dislocation density

$$\delta = \frac{1}{D^2} \tag{2}$$

Microstrain

$$\varepsilon = \frac{\beta Cos\theta}{4} \tag{3}$$

where λ = X-ray wavelength, β = FWHM (in radians, after instrumental correction) and θ = Bragg angle. The average crystallite sizes of LCM1, LCM2, LCM3, and LCM4 MOFs are 12, 30, 36, and 67 nm, respectively, indicating a clear trend of growth with varying processing conditions. The smallest crystallites (12 nm) exhibit significant quantum confinement and a large fraction of grain boundaries, while the larger crystallites (67 nm) indicate improved coalescence and enhanced structural ordering. The corresponding microstrain values of LCM1, LCM2, LCM3 and LCM4 MOFs are 7.6×10^{-3}, 1.4×10^{-3}, 1.1×10^{-3}, and 2.6×10^{-3}, respectively, revealing that lattice distortion is strongly size-dependent. The highest strain in the smallest crystallites reflects dominant internal stresses and lattice distortions, whereas its reduction with increasing size suggests relaxation of these stresses and better lattice periodicity. A slight increase at the largest size may be attributed to defect redistribution or secondary interactions during growth. Similarly, the dislocation density values of LCM1, LCM2, LCM3 and LCM4 MOFs are 2.6×10^{-3}, 1.1×10^{-3}, 0.9×10^{-3}, and 0.4×10^{-3}, respectively, showing an inverse correlation with crystallite size, confirming that smaller crystallites accommodate more defects, while larger ones possess improved crystalline quality. Further, the Williamson-Hall (W—H) equation is used to calculate the size/strain contribution of LCM1, LCM2, LCM3, and LCM4 MOFs using the equation.

$$\beta Cos\theta = \frac{n\lambda}{D} + 4\varepsilon Sin\theta \tag{4}$$

To construct the WH plot, the term βCosθ is plotted on the y-axis against 4Sinθ on the x-axis (Fig. 2). The resulting plot should yield a straight line of the form y = ax - b. Here, a = ε represents the strain. Once the strain is obtained, the residual stress in the material can be calculated using Hook's law, given as.

$$\sigma = \varepsilon.E \tag{5}$$

where E is the Young's modulus of the material (taken from literature). Since the exact value of the Young's modulus of elasticity for CaMo MOF is not reported in the literature, an approximate value was estimated by considering the reported moduli of its constituent phases. Specifically, the Young's modulus of Ca-MOF has been reported as ~11.6 GPa, while that of Mo is ~7.8 GPa. By combining these values, the effective modulus for CaMo MOF was approximated to be ~19.4 GPa [17]. Based on this reference modulus, the calculated stress for LCM1, LCM2, LCM3,

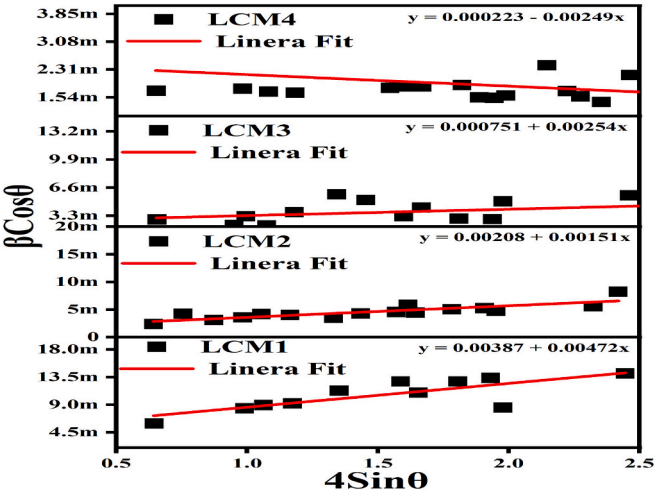

Fig. 2. WH plot of the LCM1, LCM2, LCM3 and LCM4 MOFs.

and LCM4 MOFs were found to be 9.1×10^{-2} GPa, 2.9×10^{-2} GPa, 4.9×10^{-2} GPa, and 4.8×10^{-2} GPa, respectively. These values suggest a significant reduction in the effective elastic modulus compared to the estimated bulk CaMo modulus, which may be attributed to factors such as crystallite size, microstrain, lattice distortions, and defect density within the prepared nanostructures.

Further, the structural model of the synthesized LCM1 MOF was refined against the experimental powder X-ray diffraction data using the Rietveld method. The refinement process involved simultaneous optimization of lattice parameters, atomic coordinates, scale factors, peak-shape parameters, and background contributions in order to minimize the difference between the calculated and observed diffraction intensities. The refinement profile is presented in Fig. 3(a), where the experimental data (blue crosses) are in close agreement with the calculated pattern (green line). The difference curve (cyan line) remains close to zero, and the vertical tick marks correspond to the allowed Bragg reflections of the $CaMoO_4$ phase, confirming the correctness of the structural model. The refinement converged with wR = 11.98 %, goodness-of-fit (GOF) = 1.12, and reduced $\chi^2 = 1.24$. These values fall well within the generally accepted limits for high-quality Rietveld refinements (wR < 15–20 %, $\chi^2 \approx 1$–2), indicating a robust structural fit. Fig. 3 (b) shows the reference crystal structure of the LCM1 MOF. The refined structure matches well with the JCPDS card for powellite, which crystallizes in the tetragonal scheelite-type lattice (space group $I4_1/a$, No. 88). In this framework, Mo is tetrahedrally coordinated by oxygen to form isolated MoO_4 units, while La/Ca cations occupy distorted eight-fold coordination environments. Such a configuration inherently limits direct Mo—Mo interactions, as the rigid MoO_4 tetrahedra are spatially separated and connected only through oxygen bridges. This structural feature suppresses strong exchange coupling and long-range magnetic ordering, leading instead to a soft ferromagnetic response. In addition, the low residual values and the random distribution of difference intensities demonstrate that the theoretical structural model has been reliably adjusted to match the experimental diffraction data. This confirms both the phase purity of the material and the accuracy of the refined La-substituted CaMo MOF crystal structure.

Fig. 4 shows the FT-Raman spectra of the LCM1, LCM2, LCM3 and LCM4 MOFs. The FT-Raman spectra of LCM1, LCM2, LCM3, and LCM4 MOFs provide valuable insights into the structural evolution of the MOF lattice with increasing Mo content. All samples show pronounced bands within the 100–1200 (cm^{-1}) regions. The Raman spectra of LCM1 MOF show two different active modes (A_g, and E_g) observed at (A_g) 320 and 876, (E_g) 201, 388 and 792 (cm^{-1}) corresponding to the Raman internal modes $(MoO_4)_2$ [18]. The band near 110 and 142 (cm^{-1}) is assigned to Ca^{2+} cations [19]. The above-mentioned Raman peaks show increasing

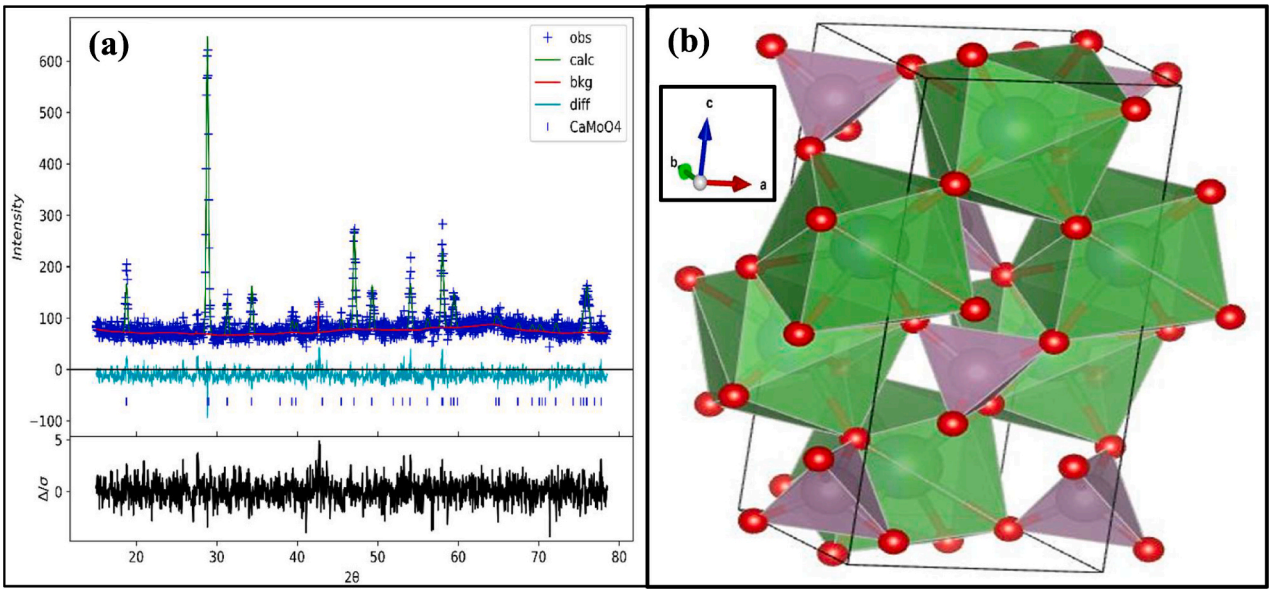

Fig. 3. (a) Rietvelt refinement pattern of the LCM1 MOF (b) Reference crystal structure of the LCM1 MOF generated from refinement data.

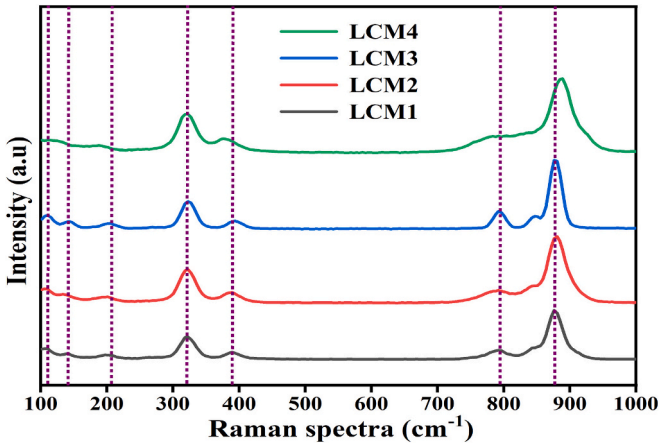

Fig. 4. FT-Raman spectra of the LCM1, LCM2, LCM3 and LCM4 MOFs.

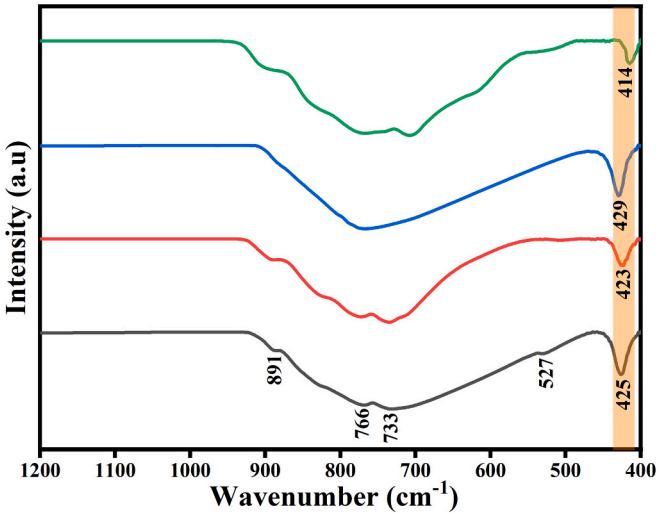

Fig. 5. FTIR spectra of the LCM1, LCM2, LCM3 and LCM4 MOFs.

intensity from LCM1 to LCM4 MOFs, suggesting stronger metal-oxygen bonding and improved crystallinity. The Raman active modes agree well with the tetragonal scheelite $CaMoO_4$ structure, consistent with the XRD results.

Fig. 5 shows the FTIR spectra of the LCM1, LCM2, LCM3 and LCM4 MOFs. All samples exhibit characteristic absorption bands in the fingerprint region (800–400 cm^{-1}). The FTIR spectra show distinct peaks at 425, 527, 733, 766 and 891 (cm^{-1}). The main bands observed at 733 and 766 (cm^{-1}) are related to the Mo—O antisymmetric stretching vibrations of $(MoO_4)_2$, while a band observed at 425 and 527 (cm^{-1}) corresponds to the absorption Ca—O band [20,21]. In addition, a band at 891 cm^{-1} is observed related to O-Mo-O asymmetric stretching vibrations [22]. It is seen that with decreasing Mo content from LCM1 to LCM4, minor shifts and intensity modulations are observed in the M-O vibrational region. These spectral changes suggest successful incorporation of Mo into the lattice, accompanied by lattice distortion or modified coordination geometries. The appearance of an additional band at ~414 cm^{-1} in LCM4, absent in the lower Mo content samples, is particularly notable. This band is attributed to Mo–O–Mo stretching vibrations, indicating the formation of molybdenum-rich clusters or altered metal-linker interactions resulting from higher substitution levels. The FTIR spectra confirm the progressive substitution of molybdenum within the calcium-based framework, influencing both the vibrational signature and the chemical stability of the material. These results are consistent with the FT-Raman and XRD results.

To gain detailed insight into the surface chemical composition and oxidation states of the elements within the synthesized LCM1, LCM2, LCM3 and LCM4 MOFs, XPS analysis of LCM1 MOF was carried out. Fig. 6a shows the survey spectra of the LCM1 MOF. The XPS survey spectra confirm the presence of carbon (C), oxygen (O), calcium (Ca), and molybdenum (Mo) peaks along with their corresponding chemical environments. Fig. 6b shows the deconvolution curve of the Ca peaks of LCM1 MOF. The Ca 2p high-resolution spectrum reveals a well-resolved spin–orbit doublet at binding energies of 347.2 eV (Ca $2p_{3/2}$) and 350.7 eV (Ca $2p_{1/2}$), with a spin-orbit splitting of approximately 3.5 eV. These values are consistent with calcium in the +2-oxidation state (Ca^{2+}) in oxide or carboxylate coordination environments [23]. Fig. 6c shows the Mo peaks of the LCM1 MOF. The Mo 3d spectrum exhibits a characteristic doublet corresponding to Mo $3d_{5/2}$ and Mo $3d_{3/2}$ at binding energies of 232.7 eV and 235.8 eV, respectively, with a spin-orbit splitting of 3.1 eV. These binding energies are attributed to molybdenum in the +6 oxidation state (Mo^{6+}), consistent with MoO_3-like

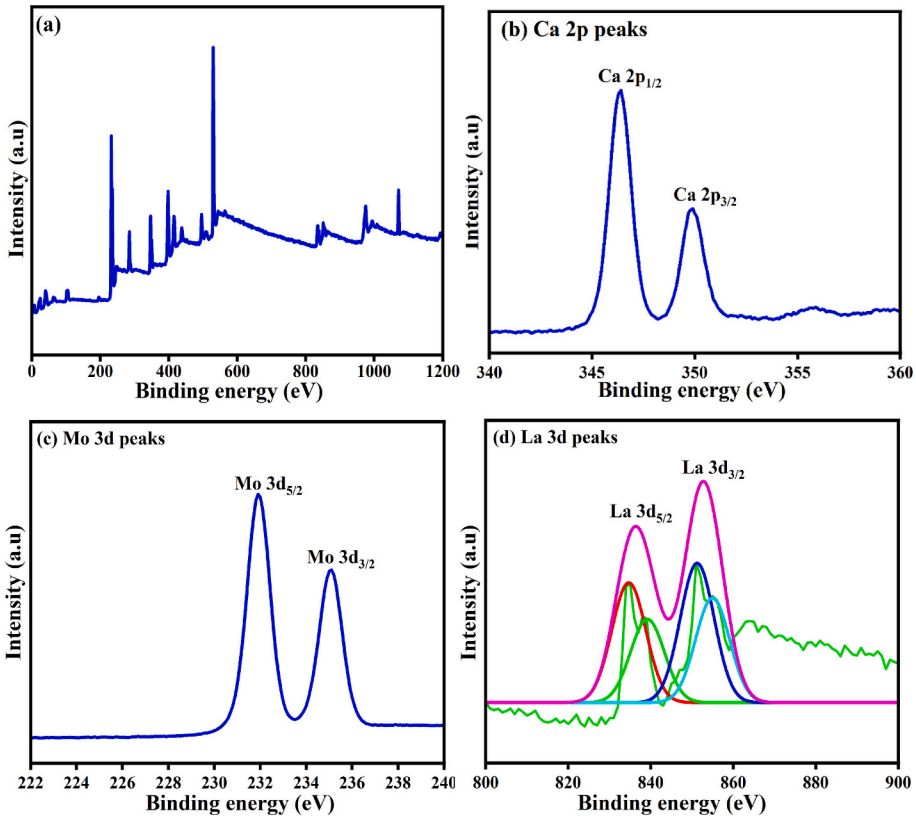

Fig. 6. (a) XPS survey, deconvolution curves of (b) Ca 2p peaks (c) Mo 3d peaks (d) La 3d peaks of the LCM1 MOF.

coordination environments [24]. The absence of additional peaks or shoulders suggests no detectable presence of Mo in lower oxidation states (e.g., Mo^{4+} or MoO), confirming that Mo^{6+} has been successfully incorporated into the framework without reduction. Fig. 6d shows the high-resolution XPS spectrum of La 3d peaks. The La peaks are observed at 834.7 eV (La $3d_{5/2}$) and 851.5 eV (La $3d_{3/2}$), which correspond to the spin-orbit components of trivalent lanthanum [25]. The presence of additional satellite structures near both main peaks is characteristic of La^{3+} species, arising from final-state effects such as shake-up processes. These results confirm the oxidation state of lanthanum as +3, indicating its stable chemical integration in the oxide lattice or framework without reduction or phase segregation. These deconvolution curves show successful substitution of La and Mo in the LCM1, LCM2, LCM3 and LCM4 MOFs.

The surface morphology of the LCM1, LCM2, LCM3 and LCM4 MOFs was systematically examined by SEM (Fig. 7). The images reveal agglomerated spherical particles of all the MOFs. It is seen that with increasing La incorporation, the spherical domains become more distinct and well-defined, while the reduction in Mo content leads to stronger clustering and agglomeration. This progressive morphological change from LCM1 to LCM4 highlights the critical role of the La/Mo ratio in governing self-assembly behavior, and this structural variation has direct implications for their magnetic properties. Fig. 8(a, b) shows TEM images of LCM1 MOF. The TEM images resemble the SEM images, which determines the consistency of results from a morphological point of view. Fig. 8(c) shows the HRTEM images of the LCM1 MOF. The HRTEM reveals that well-resolved lattice fringes are visible within the particles, with fringe spacings of 0.324 nm for the high intensity peak corresponding to (1 1 2) *hkl* planes. Fig. 8(d) shows the SAED pattern of the LCM1 MOF. The crystallite sizes calculated from XRD using the Debye-Scherrer equation are in close agreement with those obtained from TEM analysis (using ImageJ software inserted in Fig. 8c), confirming the nanoscale dimensions of all LCM MOFs. The TEM micrographs combined with SAED patterns revealed predominantly polycrystalline particles with sharp concentric rings and occasional discrete spots, consistent with randomly oriented nanocrystals interspersed with a few larger crystallites. The average particle sizes measured by ImageJ (approximately 6–8 nm) closely match the XRD-derived crystallite sizes, indicating that most particles are single crystalline.

The magnetic behavior of the LCM1, LCM2, LCM3 and LCM4 MOFs was thoroughly investigated via VSM at room temperature, as shown in Fig. 9(a) with a detailed low-field inset in Fig. 9(b). All the LCM1, LCM2, LCM3, and LCM4 MOFs exhibit symmetric S-shaped hysteresis curves typical of soft magnetic materials. Notably, LCM4 with the highest Mo content achieves the greatest saturation magnetization (Ms ≈ 0.012 emu/g), followed sequentially by LCM3 (−0.0085), LCM2 (−0.0039), and LCM1 (−0.0024). This progressive Ms. enhancement is attributed to the increase in Mo doping, which enhances magnetic exchange in LCM1, LCM2, LCM3, and LCM4 MOFs. Fig. 10(a, b) Mo content versus magnetization and magnetic retentivity of the LCM1, LCM2, LCM3 and LCM4 MOFs. The plot shows that magnetization varies nonlinearly with Mo content. As Mo decreases and La correspondingly increases, the magnetization initially remains negative, suggesting weak diamagnetic or antiferromagnetic behavior. At 7 % Mo, magnetization reaches a sharp positive peak, indicating enhanced ferromagnetic ordering. However, further decrease to 6 % Mo again leads to strong negative magnetization, reflecting instability or competing magnetic interactions between Mo and La ions. This non-monotonic trend suggests that magnetic ordering is highly sensitive to the La/Mo ratio in the LCM MOFs. Fig. 10(b) shows magnetic retentivity vs Mo content of the LCM1, LCM2, LCM3 and LCM4 MOFs. Here, magnetic retentivity increases consistently as Mo content decreases. At higher Mo concentrations (9–8 %), retentivity is very low, indicating weak magnetic ordering. With decreasing Mo and increasing La (7–6 %), retentivity increases significantly, indicating stronger ferromagnetic contributions and stabilization

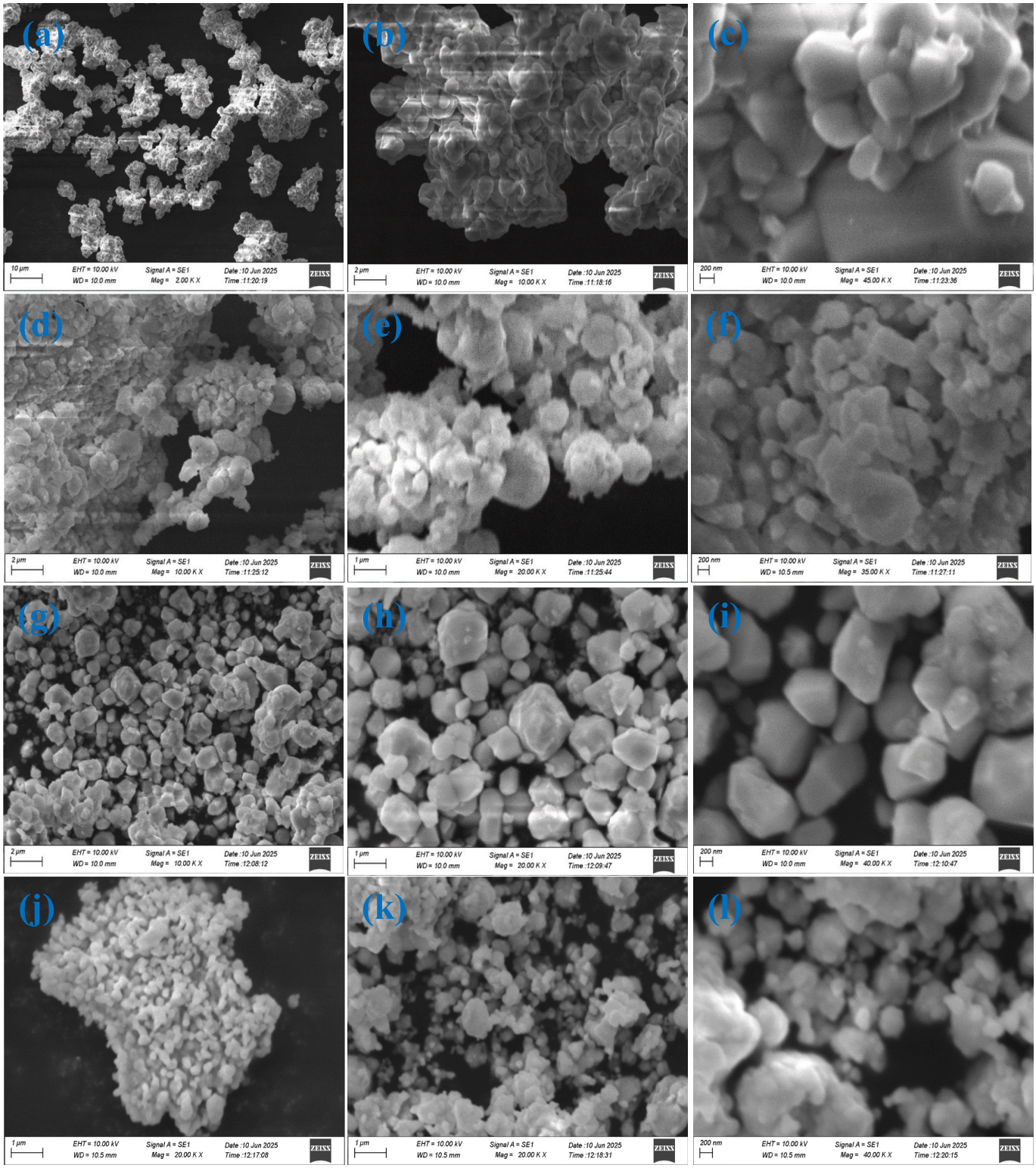

Fig. 7. SEM images (a-c) LCM1, (d-f) LCM2, (g-i) LCM3, and (j-l) LCM4 MOFs.

of magnetic domains. The increase in the Mo content induces magnetism through superexchange coupling across Mo-O-M bridge networks, and the possibility of tuning magnetic order through metal-site substitution, which in turn enables LCM MOF materials to transition from diamagnetic to soft ferromagnetic regimes [26,27]. The expanded low-field hysteresis loops show consistently low coercivity (Hc) across all the LCM1, LCM2, LCM3, and LCM4 MOFs, confirming their soft magnetic nature with minimal energy loss. The enhanced Mr. is also increased with Mo content from LCM1 to LCM4, indicating improved spin alignment retention at zero field. The transformation from near-nonmagnetic (LCM1) to moderately magnetic (LCM4) material highlights the compositional tuning of magnetic behavior through Mo substitution. This demonstrates that non-magnetic MOFs can be functionally modified to exhibit soft ferromagnetic character. The Mo incorporation into

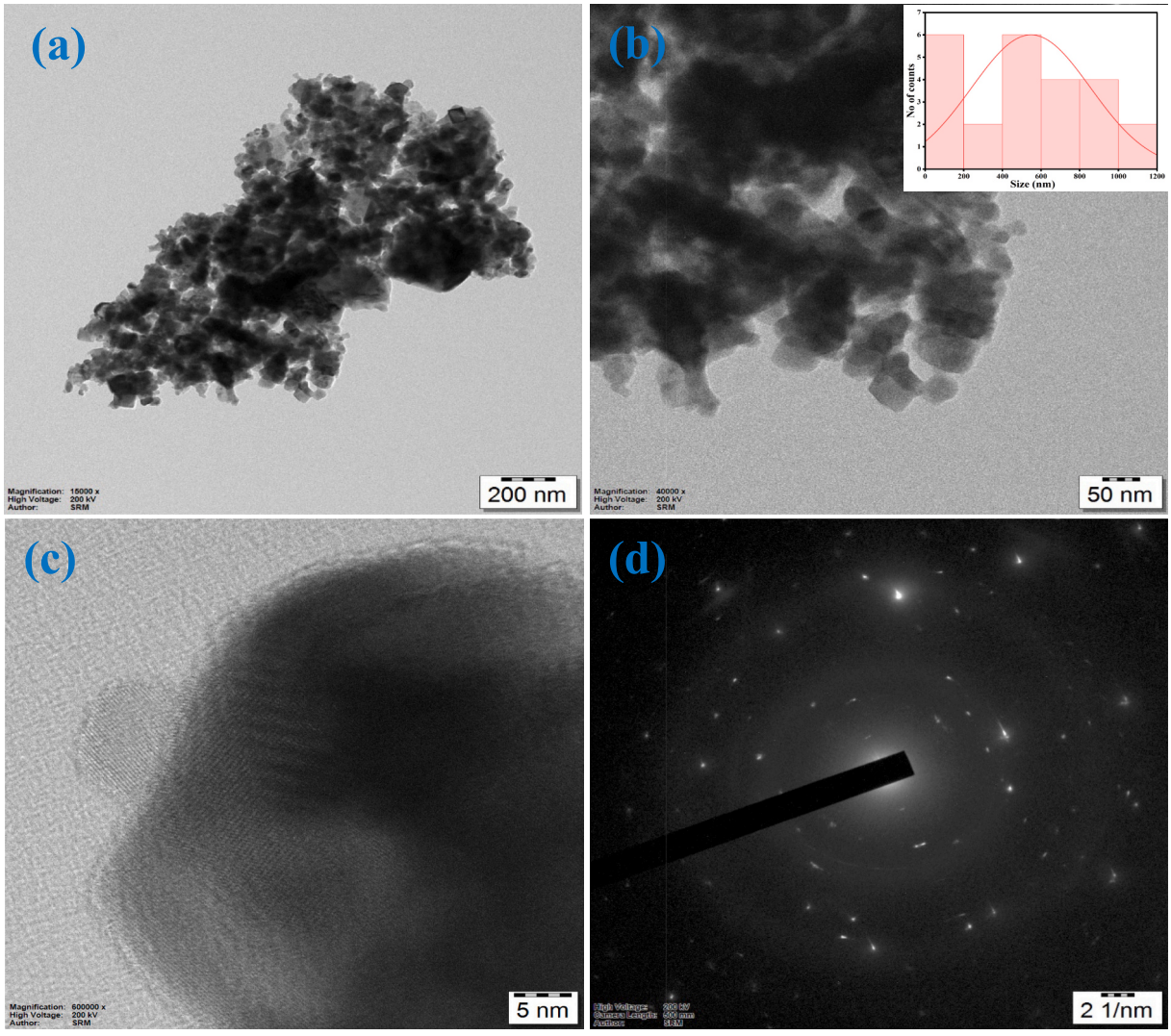

Fig. 8. (a, b) TEM images (c) HRTEM images and (d) SAED pattern of the LCM1 MOFs.

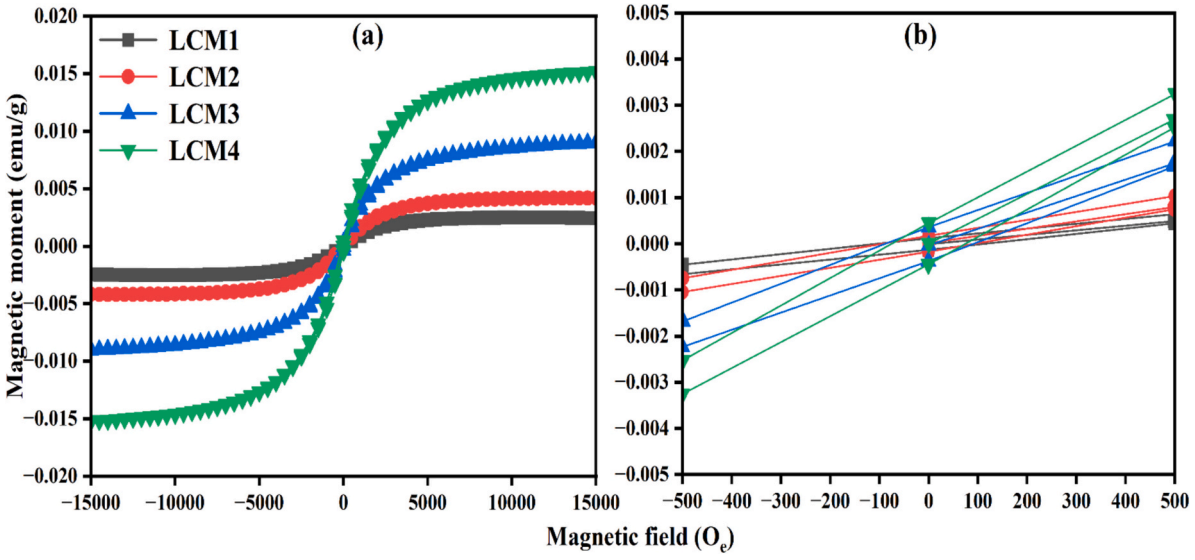

Fig. 9. (a) Hysteresis loops (b) enlarged hysteresis loops from −500 to 500 magnetic field of the LCM1, LCM2, LCM3 and LCM4 MOFs.

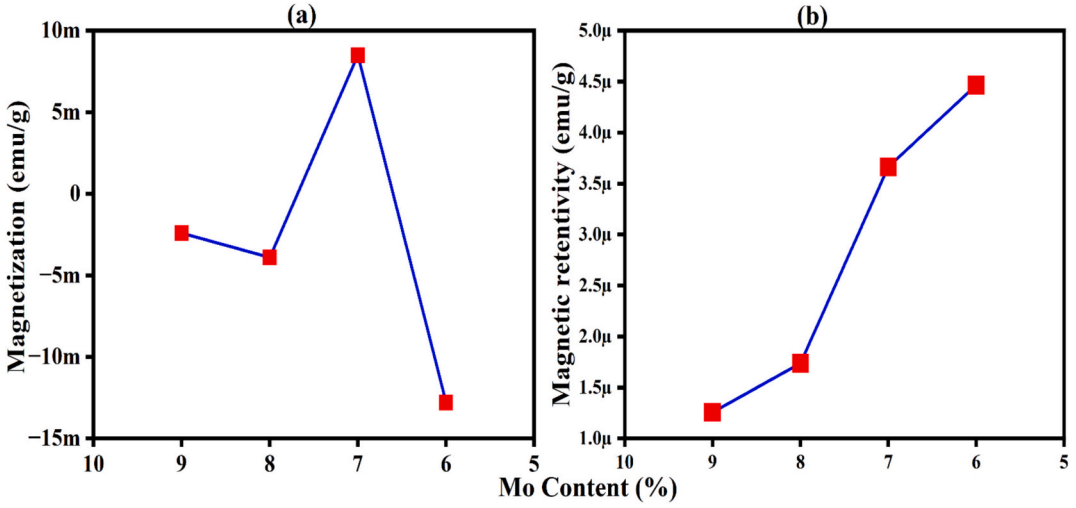

Fig. 10. (a) Mo Content versus magnetization (b) Mo content versus Magnetic retentivity of the LCM1, LCM2, LCM3 and LCM4 MOFs.

calcium-based MOFs steadily enhances both saturation (Ms) and remanent (Mr) magnetization while maintaining low coercivity, illustrating that Mo plays a key role in establishing soft magnetic order through superexchange pathways. These results align closely with recent studies on Mo-doped oxides and emerging magnetic MOF research, revealing a promising avenue for engineering magnetic functionality in porous frameworks [28,29].

4. Conclusion

In summary, we have successfully synthesized and comprehensively characterized a new series of La-substituted-CaMo MOFs. The La-substituted CaMo MOFs are characterized using various experimental techniques, including XRD, FTIR, Raman, XPS, SEM, and TEM studies. The XRD confirmed the formation of a single-phase tetragonal scheelite-type structure with a crystalline size of 12, 30, 37 and 67 (nm). The FTIR spectra show the peaks of both Ca—O and Mo—O bands. The SEM/TEM images show spherical agglomerates with increasing diameter. The XPS spectra validated the oxidation states of Ca^{2+}, Mo^{6+}, and La^{3+} elements, confirming the substitution of La ions for CaMo MOF. The VSM measurements showed a systematic increase in magnetization from 0.002 to 0.018 emu/g for LCM1 to LCM4 MOFs, confirming their soft ferromagnetic nature.

5. Key findings

- La substitution in CaMo successfully produced a single-phase tetragonal scheelite-type structure with crystallite sizes ranging between ~12 and 67 nm.
- Spectroscopic analyses (FTIR, Raman, and XPS) confirmed the incorporation of La into the CaMo lattice, leading to modifications in the local bonding and electronic environment.
- Morphological investigations (SEM and TEM) revealed uniform nanostructures with polycrystalline features, and grain size estimations from TEM were consistent with XRD results.
- Magnetic measurements demonstrated that La doping significantly affects saturation magnetization and coercivity, establishing a direct correlation between Molybdenum content and magnetic behavior.

6. Future scope

- Systematic studies on varying La doping levels and synthesis conditions could further optimize the structural and magnetic properties of CaMo-based materials.
- Exploration of electrochemical performance may expand the application potential of these materials in energy storage and catalytic systems.
- The tunable magnetic behavior suggests promising avenues for the development of multifunctional materials in spintronic and related advanced technologies.

CRediT authorship contribution statement

P. Arularasan: Writing – original draft, Visualization, Formal analysis, Conceptualization. **Saravanan Pandiaraj:** Writing – review & editing, Resources, Conceptualization. **P. Rajesh:** Writing – review & editing, Resources. **M. Pavithra:** Writing – review & editing, Resources. **G.N. Dar:** Writing – review & editing, Resources. **S.R. Majid:** Writing – review & editing, Supervision, Resources, Methodology. **Mohd Arif Dar:** Writing – original draft, Validation, Supervision, Methodology, Investigation, Formal analysis, Conceptualization.

Declaration of competing interest

The authors declare that they have no known competing financial interests or personal relationships that could have appeared to influence the work reported in this paper.

Acknowledgments

The authors extend their appreciation to the King Salman Center for Disability Research for funding this work through Research Group No. KSRG-2024-394.

Data availability

Data will be made available on request.

References

[1] C. Huang, V. Nguyen, S.-R. Zhou, S.-Y. Hsu, J.-X. Tan, K.C.-W. Wu, Metal–organic frameworks: preparation and applications in highly efficient heterogeneous photocatalysis, Sustainable Energy Fuels 4 (2) (2019) 504–516, https://doi.org/10.1039/C9SE00972H.
[2] V.F. Yusuf, N.I. Malek, S.K. Kailasa, Review on metal−organic framework classification, synthetic approaches, and influencing factors: applications in energy, Drug Deliv. Wastewater Treatm. (2022), https://doi.org/10.1021/acsomega.2c05310.
[3] M. Orts-Arroyo, R. Rabelo, A. Carrasco-Berlanga, N. Moliner, J. Cano, M. Julve, F. Lloret, G. De Munno, R. Ruiz-García, J. Mayans, J. Martínez-Lillo, I. Castro, Field-induced slow magnetic relaxation and magnetocaloric effects in an oxalato-

bridged gadolinium (III)-based 2D MOF, Dalton Trans. 50 (11) (2021) 3801–3805, https://doi.org/10.1039/D1DT00462J.
[4] I.S. Imaduddin, S.R. Majid, N.H. Idris, et al., Electrochemical and ion-kinetics performances of BMOF-derived Co_3O_4/CaO cathodes for calcium-ion batteries, Ionics 31 (2025) 3451–3465, https://doi.org/10.1007/s11581-024-06056-5.
[5] D. Kanakaraju, M.A.A. Bin Jasni, Y. Lim, A highly photoresponsive and efficient molybdenum-modified titanium dioxide photocatalyst for the degradation of methyl orange, Int. J. Environ. Sci. Technol. 19 (2021), https://doi.org/10.1007/s13762-021-03484-y.
[6] Z.K. Heiba, M.B. Mohamed, A.M. Wahba, Effect of Mo substitution on structural and magnetic properties of Zinc ferrite nanoparticles, Journal of Molecular Structure 1108 (2016) 347–351. https://doi.org/10.1016/j.molstruc.2015.12.042.
[7] M.A. Dar, S.R. Majid, S. Sarkar, et al., Synthesis and characterization of binder-free Ni, Cu, Mn, and Co metal–organic frameworks for supercapacitors, Ionics 31 (2025) 3715–3726, https://doi.org/10.1007/s11581-025-06138-y.
[8] X. Guan, Y. Ren, S. Chen, J. Yan, G. Wang, H. Zhao, C. Liu, Charge separation and strong adsorption-enhanced MoO3 visible light photocatalytic performance, Journal of Materials Science 55 (14) (2020) 5808–5822. https://doi.org/10.1007/s10853-020-04418-8.
[9] M.B. Mohamed, A.M. Wahba, M. Yehia, Structural and magnetic properties of CoFe2− xMoxO4 nanocrystalline ferrites, Materials Science and Engineering: B 190 (2014) 52–58. https://doi.org/10.1016/j.mseb.2014.09.010.
[10] G.D. Dwivedi, K.F. Tseng, C.L. Chan, P. Shahi, J. Lourembam, B. Chatterjee, S. Chatterjee, Signature of ferroelectricity in magnetically ordered Mo-doped CoFe 2 O 4. *Physical Review B—Condensed*, Matter and Materials Physics 82 (13) (2010) 134428. https://doi.org/10.1103/PhysRevB.82.134428.
[11] K. Murai, K. Yamashita, G. Kitahara, M. Tokuda, A. Yoshiasa, Syntheses, single crystal structure analyses and ultraviolet light emission of $CaW_{1-x}Mo_xO_4$ (x = 0.0–1.0) scheelite–powellite solid solutions, J. Mineral. Petrol. Sci. 118 (1) (2023). https://doi.org/10.2465/jmps.220901.
[12] HF. Zhai, W. Li, J. Zhang, et al., Excitation-induced tunable luminescent properties of polyhedral $CaMoO_4$ microcrystallites, J Mater Sci: Mater Electron 32 (2021) 10008–10017. https://doi.org/10.1007/s10854-021-05659-2.
[13] A. Azulay, T. Leibovitz, Y. Natanzon, O. Zabari, Y. Amouyal, Ca3Mn2O7-layered perovskites: Effects of La-and Y-doping on phase stability, microstructure, and thermoelectric transport, Journal of the American Ceramic Society 106 (1) (2023) 213–226. https://doi.org/10.1111/jace.18753.
[14] Zhenli Tao, Jiamao Li, Junxian Wang, Yuxuan Ren, Xiangkai Zhu, Yunfeng Guo, Zexing Wang, Wenbo Wang, Sintering, microstructure and microwave dielectric properties of Ca3Co2SiV2O12 through inequivalent substitution of Ca2+ with La3+, Ceramics International, 51, 19, 2025, 29744-29751. https://doi.org/10.1016/j.ceramint.2025.04.177.
[15] A.L. Pellegrino, P. Cortelletti, M. Pedroni, A. Speghini, G. Malandrino, Nanostructured CaF2: Ln3+ (Ln3+= Yb3+/Er3+, Yb3+/Tm3+) thin films: MOCVD fabrication and their upconversion properties, Advanced Materials Interfaces 4 (18) (2017) 1700245. https://doi.org/10.1002/admi.201700245.
[16] R. Meenambal, R.K. Singh, P.N. Kumar, S. Kannan, Synthesis, structure, thermal stability, mechanical and antibacterial behaviour of lanthanum (La^{3+}) substitutions in β-tricalcium phosphate, Mater. Sci. Eng. C 44 (2014) 243–251, https://doi.org/10.1016/j.msec.2014.07.054.
[17] T. Kamencek, E. Zojer, Understanding the anisotropic elastic properties of metal–organic frameworks at the nanoscale: the instructive example of MOF-74, J. Phys. Chem. C 125 (44) (2021) 24728–24745, https://doi.org/10.1021/acs.jpcc.1c07882.
[18] Palanisamy Rajkumar, Vediyappan Thirumal, Akshaya Subhramaniyan Rasappan, Maalavika S. Iyer, Sankaiya Asaithambi, Kisoo Yoo, Jinho Kim, Electrochemically enhanced battery-type Ni substituted CaMo-MOF electrodes: Towards futuristic energy storage system, J. Energy Stor. 80 (2024) 110284, 2352-152X, https://doi.org/10.1016/j.est.2023.110284.
[19] H.F. Zhai, W. Li, J. Zhang, et al., Excitation-induced tunable luminescent properties of polyhedral $CaMoO_4$ microcrystallites, J. Mater. Sci. Mater. Electron. 32 (2021) 10008–10017, https://doi.org/10.1007/s10854-021-05659-2.
[20] Zhiyao Hou, Ruitao Chai, Milin Zhang, Cuimiao Zhang, Peng Chong, Xu Zhenhe, Guogang Li, Jun Lin, Fabrication and luminescence properties of one-dimensional CaMoO4: Ln^{3+} (Ln= Eu, Tb, Dy) nanofibers via electrospinning process, Langmuir 25 (20) (2009) 12340–12348, https://doi.org/10.1021/la9016189.
[21] Titipun Thongtem, Anukorn Phuruangrat, Somchai Thongtem, Characterization of $MMoO_4$ (M= Ba, Sr and Ca) with different morphologies prepared using a cyclic microwave radiation, Mater. Lett. 62 (3) (2008) 454–457, https://doi.org/10.1016/j.matlet.2007.05.059.
[22] T.D. Nguyen, A. Worrad, D. Thirulogachandar, F.E. Celik, S. Caratzoulas, G. Tsilomelekis, Insights into the molecular structure of MoOx catalysts via static and transient Raman experimentation, J. Phys. Chem. C (2024), https://doi.org/10.1021/acs.jpcc.4c02018.
[23] J.-G. Choi, L.T. Thompson, XPS study of as-prepared and reduced molybdenum oxides, Appl. Surf. Sci. 93 (1996) 143–149, https://doi.org/10.1016/0169-4332(95)00317-7.
[24] M. Zhang, W. Wu, J. Luo, H. Zhang, J. Liu, X. Liu, X. Lu, A high-energy-density aqueous zinc–manganese battery with a La-Ca co-doped ε-MnO_2 cathode, J Mater Chem A 8 (23) (2020) 11642–11648, https://doi.org/10.1039/D0TA03706K.
[25] A.A. Yadav, V.C. Lokhande, R.N. Bulakhe, et al., Amperometric CO_2 gas sensor based on interconnected web-like nanoparticles of La_2O_3 synthesized by ultrasonic spray pyrolysis, Microchim. Acta 184 (2017) 3713–3720, https://doi.org/10.1007/s00604-017-2364-3.
[26] O. Mirzaee, A. Shafyei, M.A. Golozar, H. Shokrollahi, Influence of MoO_3 and V_2O_5 co-doping on the magnetic properties and microstructure of a Ni–Zn ferrite, J. Alloys Compd. 462 (1–2) (2008) 148–152, https://doi.org/10.1016/j.jallcom.2007.06.120.
[27] S.W. Hyun, C.S. Kim, Superexchange interactions in inverse spinel lithium ferrites, Phys. Status Solidi B 244 (15) (2007) 5474–5480, https://doi.org/10.1002/pssb.200777209.
[28] F. Al-Mokdad, Z. Bitar, R. Sayed Hassan, N. Yaacoub, R. Awad, Effect of molybdenum doping on the structural and magnetic properties of $MnFe_2O_4$ magnetic nanoparticles, Appl. Phys. A *126*, Article 566 (2020), https://doi.org/10.1007/s00339-020-03687-z.
[29] *In situ*-growth Mo-doped MOFs-derived phosphide supported nanosheets as efficient bifunctional electrocatalyst towards urea-water electrolysis, New J. Chem. (2023), https://doi.org/10.1039/d3nj01301d.